



Evaluation of Shear Stress Augmentation Over Large-Scale Roughness Using Pressure Sensitive Paint

Wesley J Condren! Chris Hambidge! David Steuer! Anthony Finnerty! Matthew McGilvray 1

Abstract

Roughness effects are of significant importance in the design of ablative thermal protection systems for atmospheric entry. In particular, the augmentation of skin friction increases the drag experienced by the vehicle. The drag over rough walls is a sum of both viscous and pressure effects, the latter dominating in the fully rough regime. Furthermore, these effects are typically understood through empirical correlations developed at subsonic conditions. This paper presents an experimental study into roughness-induced shear stress augmentation in hypersonic flow. The experiments were conducted in the Oxford High Density Tunnel at Mach 5 with a unit Reynolds number ranging from 44 - $60 \times 10^6 \text{m}^{-1}$ and a roughness Reynolds number well within the fully rough regime. Pressure sensitive paint was used to evaluate a spatially continuous surface pressure map over the roughness elements. Through integration, the pressure drag over the surface is calculated and compared to a direct shear stress measurement using a floating force balance.

1. Nomenclature Nomenclature

Latin

A – Area

 C_d – Drag Coefficient C_f — Fiction Coefficient F — Force

I – Intensity

k - Roughness Height

 k^+ - Roughness Reynolds Number

M – Mach Number

p – Pressure

Re - Reynolds number T – Temperature

u – Velocity

 U_{τ} – Friction Velocity

x – Distance along the plate

 \bar{x} – x distance normalised by sawtooth length

X – Fitting parameter

 $y\,$ – Distance across the plate

Y - Fitting parameter

Z – Fitting parameter

Greek

 δ – Boundary Layer Height

 θ – Angle

 μ – Dynamic viscosity

 ρ – Density τ – Shear Stress

Subscripts

C# – At condition number #

fp - Flat Plate

 k^+ – Rough wall value

l – Leeward p – Pressure r – Recovery

ref – At reference condition

s – Sand-grain w – Windward

wall - Value at the wall ∞ – Free stream value

2. Introduction

The loss of mass during re-entry from an ablative heat shield plays a crucial role in maintaining subcritical temperatures of the hypersonic vehicle's surface. However, the ablation process of typical ablative materials such as carbon-carbon or carbon-phenolic composites is highly non uniform, occurring on many

¹University of Oxford, Thermofluids Institute OX2 0ES, Oxford, United Kingdom, Corresponding author email address: wesley.condren@eng.ox.ac.uk.

different scales and at different rates [1, 2]. Consequently, surface roughening is an unavoidable effect of ablative TPS. The roughening of the wall during flight subsequently results in the enhancement of turbulent motions in the boundary-layer, promoting laminar-to-turbulent transition [3, 4]. Additionally, surface roughness greatly augments shear stress above smooth wall levels, further increasing surface recession via spallation [5] and affecting vehicle stability [6]. It is thus of high importance to understand rough wall effects in hypersonic flow fields.

The primary body of work on rough wall flows was conducted in closed channel water or low speed air flows. The pioneering work of Nikuradase on sand-grain roughness and then the expansion of that work by Schlichting defined sand-grain roughness height k_s and sand-grain roughness Reynolds number k_s^+ as key scaling parameters for rough wall effects [7, 8]. Following this, Goddard explored rough wall effects, namely the shear augmentation in compressible flow with an adiabatic wall, and found that the data still correlated well with the logarithm of k_s^+ at these speeds [9]. Similar works by Wade, Reda and Youngs on v-grove roughness patterns came to the same conclusion with a slight modification to account for non adiabatic walls [10, 11, 12]. However, in each of these works, the height of the roughness elements remained small compared to the boundary layer thickness $k/\delta < 0.07$ [13]. At higher Mach and Reynolds numbers, the boundary layer thins, resulting in roughness elements protruding into the sonic line. In these conditions, a departure from the behaviour seen in earlier works is observed. Holden's work on slender cones with an edge Mach number of 2-8 [14] showed that heating was underpredicted by Powars correlation [15] [16]. The work on patterned HEEET-like roughness by Wilder and Prabhu [17] observed that the equivalent sand-grain analysis worsened the agreement to theory for their largest roughness scale ($k/\delta = 0.2$). This was seconded by Hambidge *et.al.* which showcased significant shear augmentations [18]. Ultimately, large-scale rough wall effects are present during re-entry and have been shown to scale differently from current rough wall theory but remain relatively unstudied.

Utilising the dominance of form drag within the fully rough regime, this work presents pressure sensitive paint (PSP) as a means to acquire drag coefficients and thus shear augmentation factors over rough walls in hypersonic flow. The testing was completed in the Oxford High Density Tunnel in a Mach 5 turbulent boundary layer using a large-scale, two-dimensional sawtooth roughness pattern. The PSP method is compared to a direct shear stress measurement using a force balance used in previous rough wall work [18]. The advantage of PSP over conventional force measurements is that it also provides a non-intrusive, spatially continuous pressure field over the surface. As roughness effects are often attributed to alteration in fluid motion, the pressure field, which can be used to infer flow features, is of particular interest to rough wall work.

3. Measurement Techniques

3.1. PSP

Pressure sensitive paint (PSP) is an optical technique that utilises on the interaction between oxygen and the fluorescence of specific molecules dispersed in a binder to determine the pressure over a surface. The fluorescent molecules known as luminophores, when excited by a particular wavelength of light to a higher energy state, de-excite through the emission of photons at characteristic wavelengths. The presence of oxygen provides a non radiative pathway for the luminophore to return to ground state, consequently reducing the intensity of its fluorescence. This drop in intensity is proportional to the concentration of oxygen and thus its partial pressure. Finally, provided that the gas composition is known and remains constant, the intensity signal scales directly with the local static pressure.

The PSP signal is dependent on a plethora of different environmental factors, such as temperature and humidity. Moreover, the degree to which these factors alter the signal is dependent on the type of luminophore, choice of binder, and application method. In this work, anodised aluminium PSP (AA-PSP) with Ruthenium-tris(4,7-diphenyl-1,10-phenanthroline) ([Ru(dpp) $_3$] $^{2+}$) as the luminophore was used. AA-PSP, developed by Asai *et.al* [19] and further improved by Sakaue [20, 21], binds directly to the porous micro-structure of the model that is either created by the anodisation or is innate to the material such as a porous ceramic like alumina [22]. This binding significantly increases the response time of the paint [23] — an important parameter for short duration hypersonic testing. Dichloromethane was selected as the solvent as it produces greater pressure sensitivity in the paint [24]. The concentration

of the ruthenium complex and dichloromethane solution was set to 0.3mM in accordance to the findings of Ref.[25]. Concentrations of this magnitude were found to have the highest pressure sensitivity and signal level without a significant increase in tempature effects. The paint was then applied to the surface via airbrush, keeping a constant distance between the paint and the sample. Prior to the application, the surface was cleaned thoroughly with IPA and allowed to dry to remove surface impurities that may affect the binding of PSP.

3.2. Force Balance

The force balance used in this work was developed and presented by Steuer *et al.*. Reference [26] details the design and calibration of the device in more depth than provided in this paper. The shear module utilises a modular floating element design allowing for multiple 3-D surfaces to be tested. The modular surface element is 132.7x89.6mm and the overall force balance dimensions are 310x110x68mm allowing it to be mounted within the flat plate such that the floating element is centred at x = 350mm. Figure.1 highlights the core components of the module. When subject to the high speed flow, the floating element moves as a result of the interaction between it and the flow. A low friction *Hepco Motion* AU1213L300P1 linear slide ensured the unimpeded, single axis motion of the element parallel to the flow direction. The resultant force is then recorded by a *Interface* SMT S-Type 10N load cell. The floating surface is connected to the rest of the device through a rigid brass tray. The high stiffness of the brass prevents the deformation of the tray under load, further restricting motion to a single axis. Additionally, the interface between the brass and the surrounding aluminium form a labyrinth seal to prevent interference from any internal pressure differentials that may be generated during testing.

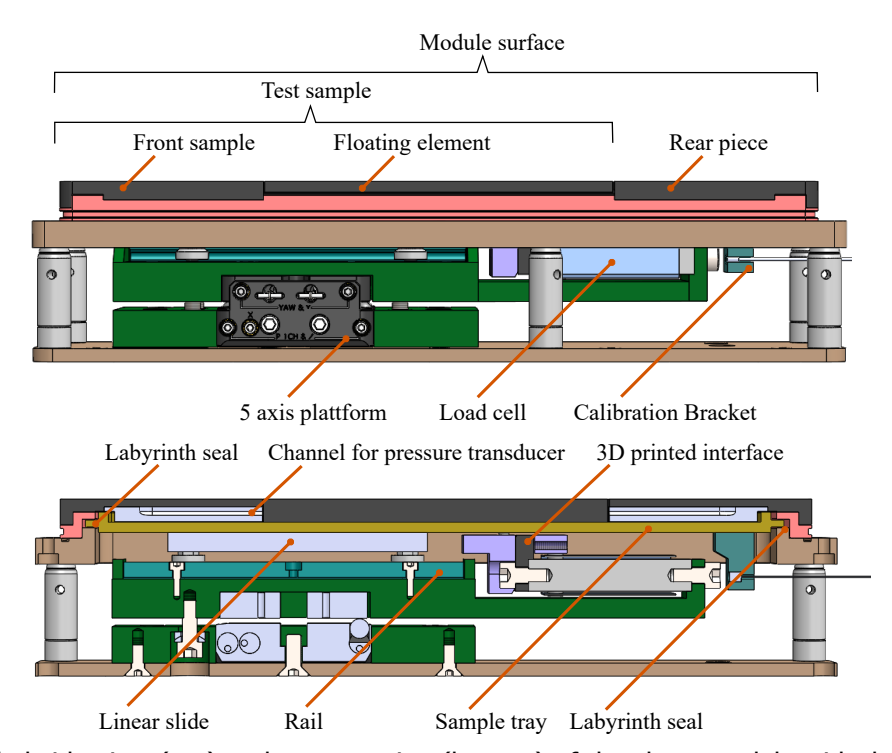


Fig 1. Detailed side view (top) and cross section (bottom) of the shear module with the smooth test surface.

The shear module evaluated the shear stress experienced by the floating element through a transient calibration, pressure correction, and acceleration compensation. The transient calibration was completed in-situ using a *PCB piezotronics* 086C01 impact hammer and a specially designed calibration surface that provided an impact site for the the hammer. The resulting signal from the load cell was deconvolved using a LSQR-algorithm detailed in Paige and Saunders [27]. The pressure correction removes the fraction of the measured force that originates from the pressure differential between the front and rear

gaps of the split sample design. Two *Kulite* XCS-062-10PSIA are used to determine the pressure within both gaps and thus the required pressure differential. The acceleration of the flat plate and therefore the resultant force that caused it was determined by assuming an idealised mass-spring system. The change in position of the flat plate was captured using high speed imaging at 1kHz and used to evaluate its acceleration through a second order central difference approximation.

4. Experimental Setup

4.1. Oxford High Density Tunnel

The experiments were conducted at the High Density Tunnel (HDT) situated in the Oxford Thermofluids Institute (Figure.2(b)). The facility operates as a Ludwieg tube, and the barrel is filled to a pressure and heated electrically to a specified temperature prior to an experiment. Once the gas has equilibrated it is passed through a fast- acting plug valve and accelerated through a contoured nozzle into an evacuated test section. HDT produces low enthalpy, high Reynolds number flows with Mach numbers ranging from 4-7 [28, 29]. Due to the unsteady flow dynamics associated with the opening of the plug valve, HDT produces a series of steady periods of total pressure and unit Reynolds numbers.

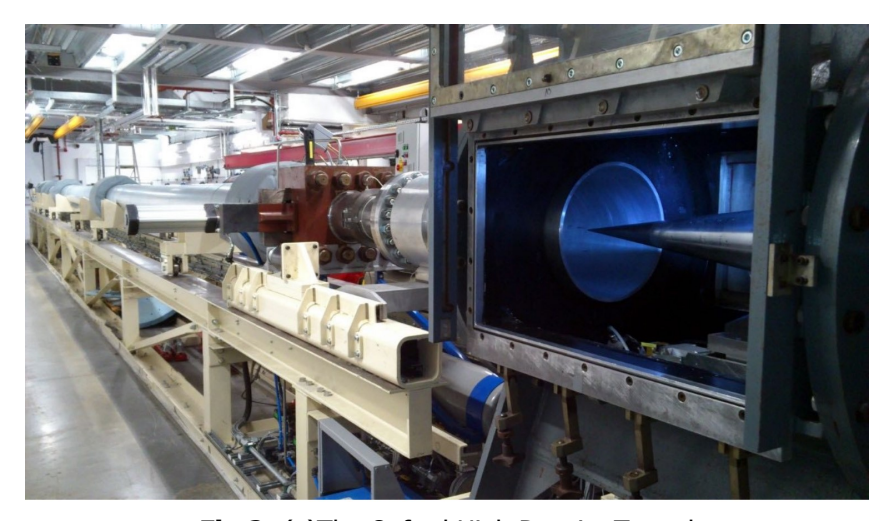


Fig 2. (a) The Oxford High Density Tunnel

4.2. Test Conditions

The test conditions averaged over the steady periods produced by HDT during the experiment are detailed in Table.1. The free stream gas composition was alternated between nitrogen and synthetic air as detailed in section.6.2. The viscosity

4.3. Flat Plate Model

The model consisted of a 575x260 mm flat plate with a sharp leading edge mounted vertically shown in Fig.3. The plate houses an interchangeable test article of nominal dimensions 290x90mm, 205mm downstream of the leading edge. To avoid flow transition effects on the test article's surface, a boundary layer trip of height 0.5mm is located 67.5mm from the leading edge. Following the trip at 85mm downstream, a thin film gauge array (TFGA) determines the state of the incoming flow. Both the test article and TFGA are aligned with the centre of the flat plate.

Units	C1	C2	C3
-	4.95	4.95	4.93
kPa	3850	2970	2330
kPa	7.6	5.95	4.75
K	438	406	376
K	74.3	68.6	64.0
ms^{-1}	870	836	805
kgm^{-3}	0.34	0.29	0.25
$10^6 m^{-1}$	58	51	44
	$^{-}$ kPa kPa K K ms^{-1} kgm^{-3}		- 4.95 4.95 kPa 3850 2970 kPa 7.6 5.95 K 438 406 K 74.3 68.6 ms^{-1} 870 836 kgm^{-3} 0.34 0.29

Table 1. Free stream conditions.

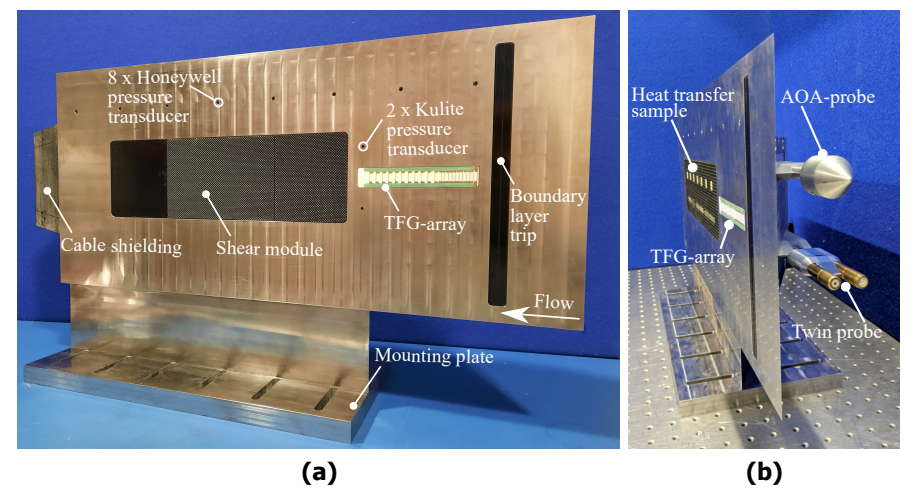


Fig 3. Flat plate model side view (a) and front view (b).

The model was instrumented with two XTL-140M-0.7BARA kulites 30mm above and below the plate's centre line, to evaluate the surface pressure 15mm prior to the test article. Beginning 90mm downstream of the leading edge, 82mm off centreline, eight *Honeywell* HSCDANN015PAAA5 sensors monitor the static pressure at 65mm intervals along the plates length. Lastly, an angle of attack (AoA) probe and a twin probe equally spaced on the underside of the model are used to determine the model alignment and pitot pressure and total temperature. The details are displayed in Fig.4.

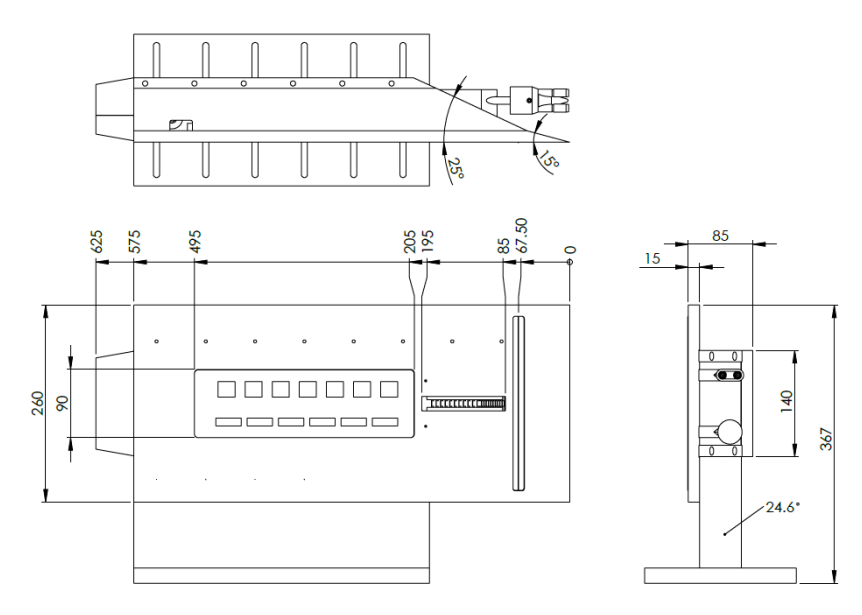


Fig 4. Schematic of the flat plate model detailing sensor locations, dimensions in mm.

4.4. Roughness Geometries

The roughness pattern used is an idealised two dimensional sawtooth pattern with a windward and leeward angle of 25 and 80 degrees respectively. The teeth have a wavelength of 2.75mm and a roughness height, k, of 1mm peak to trough. At this height, the pattern occupies approximately 20% of the boundary layer ($k/\delta \approx 0.2$) and therefore, relative to the free stream conditions, is large-scale. Figure.5 shows the pattern machined into *Metapor* CE170 and sealed into a mounting plate. The material was chosen as it exhibits a micro-porous structure similar to anodised aluminium and alumina that allows the paint to bind to the surface. The patterns were mounted into the flat plate such that the melt height, a volumetric average height, is level with the flat surface. Consequently, the trough and peaks of the pattern sit 0.5mm below and above the flat plate surface respectively. The key geometric quantities are displayed in Table.2 including the equivalent sand-grain roughness heights using van Rij, Dirling and Sigal's shape parameter correlations [30, 31, 32].

Parameter	Units	Value
k	mm	1.00
k/δ_{C2}	-	0.222
$ heta_w$	degrees	25
$^{\circ}w$	acgrees	23
θ_1	degrees	80
- 6	acgices	00
k_s (van Rij) [30]	mm	1.94
k_s (Dirling) [31]	mm	5.54
		0.00
k_s (Sigal) [32]	mm	8.00

Table 2. Sawtooth Roughness Pattern Details.

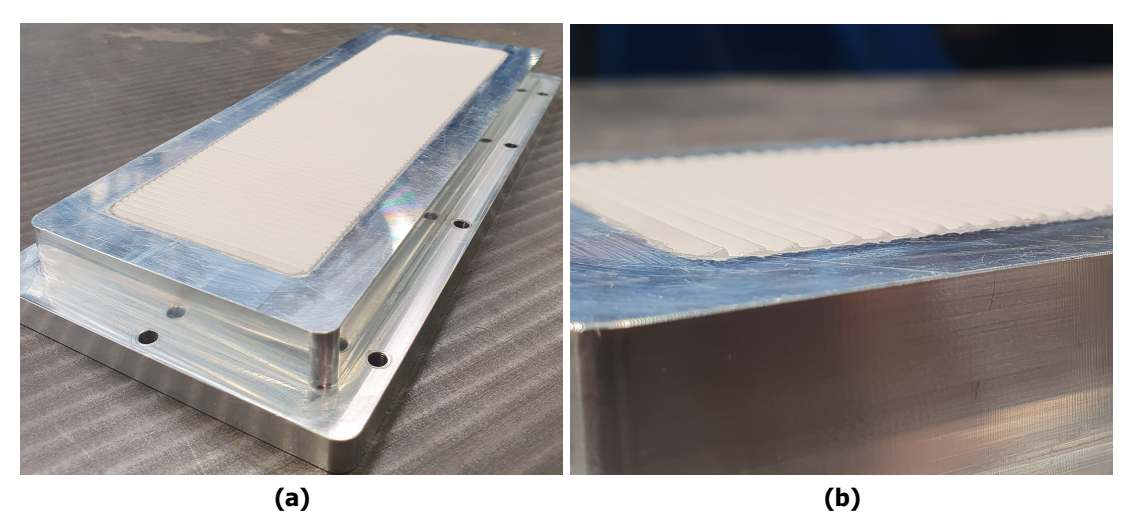


Fig 5. Roughness samples with the sawtooth geometry sealed into the mounting plate (unpainted).

5. Optical Setup

A schematic of the optical setup is shown in Fig.6. A *Luminus* PT-120-B-L11-EPG LED with a peak emission at 460nm was used as the excitation light source. The LEDs were powered by a 5A 6V power supply that, due to the high output intensity of $[Ru(dpp)_3]^{2+}$ for a given input, produced a sufficient SNR. The fluorescent light was then isolated with the use of a longpass optical filter with a cut off frequency of 550nm prior to being captured by a *Photron* AX200 high speed camera. The AX200 was operated at a frame rate of 1 kHz with a FoV of 768x768. The FoV was further cropped in post to record 383x768 pixels over the sample surface, providing a resolution of 0.12 pixels per mm.

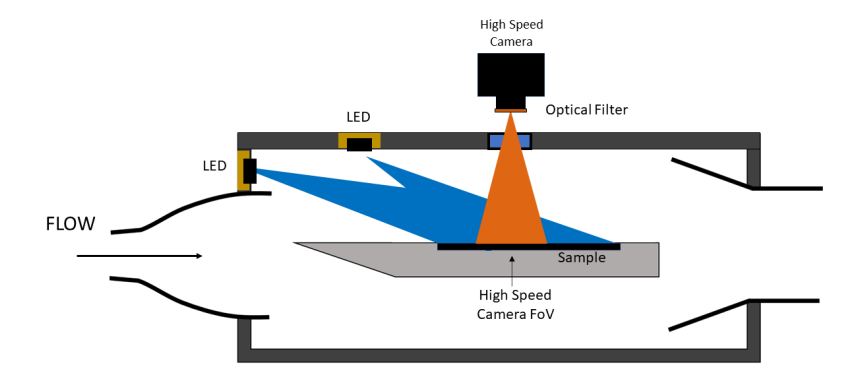


Fig 6. Schematic of the PSP optical setup.

6. PSP Post Processing

The raw intensity variation of the PSP fluorescence acquired during the test is output by the AX200 as a pixel map of counts against time. The data is then normalised by the reference intensity I_{ref} captured at reference pressure p_{ref} with no cross-flow prior to the test. The normalised intensity $\frac{I_{ref}}{I}$ is then averaged over the steady periods detailed in section.4.1 as a noise reduction measure.

6.1. LED Intensity Correction

Over the course of a test or calibration, the LED heats up. This heat alters the intensity output by the LED consequently affecting the PSP signal [22]. To account for this alteration, the LED's junction temperature is monitored by the built in thermistor during each shot and calibration. The thermistor is supplied a constant current of 100μ A, and the corresponding voltage drop is converted to a junction temperature using the thermistor specs provided by the manufacture. Next, the calculated temperature is mapped to a change in LED intensity. This conversion is completed using a LED intensity verse temperature curve acquired through a bench-top test completed in-house, shown in Fig.7. The LED was set up in-situ and supplied current as used during the calibration and test for 5 minutes. The thermistor was monitored as described above, and the intensity variation was recorded with a spectrometer placed at the same distance away from the LED as the painted surface. The PSP response is then corrected by normalising out the change in intensity from the LEDS.

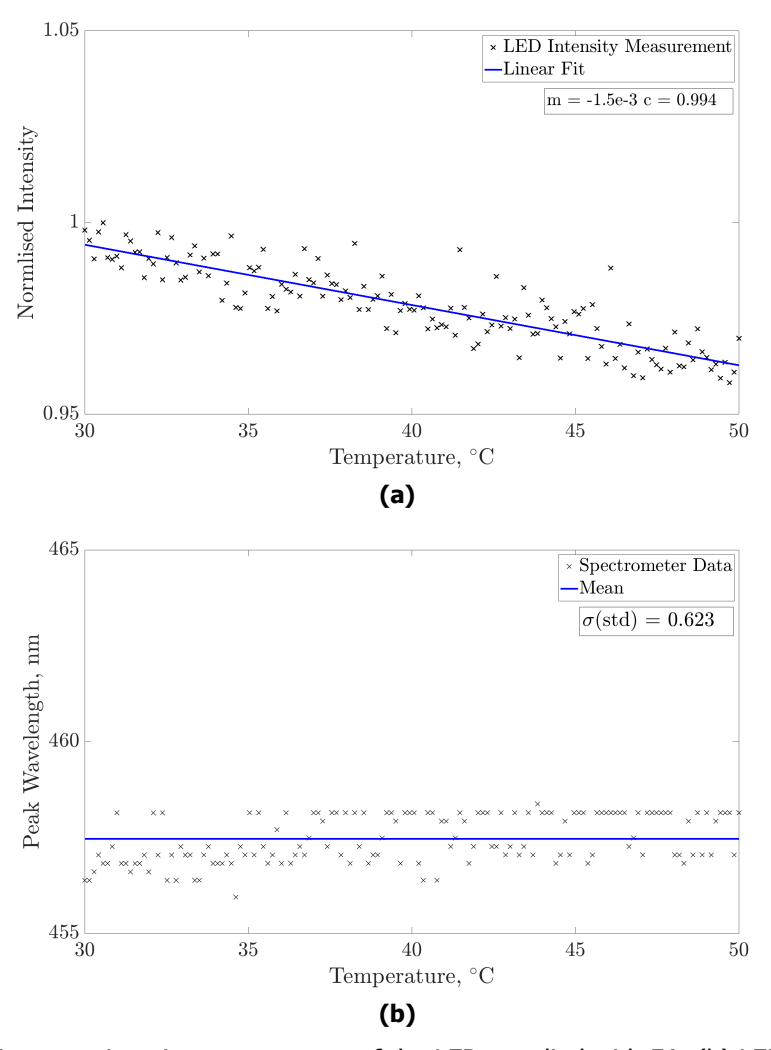


Fig 7. (a) Intensity verse junction temperature of the LED supplied with 5A. (b) LED Wavelength verse temperature supplied with 5A.

6.2. Temperature Effects

During the experiment there is an appreciable change in temperature over the surface that is further enhanced by roughness effects. As a consequence of the paints temperature sensitivity the normalised intensity described above is a function of both pressure and temperature changes during the shot.

Therefore, in order to apply a calibration curve to the signal, the desirable pressure effects must be decoupled from the temperature effects. This is done by coupling an equivalent nitrogen free stream shot for every test with an air free stream. Due to the absence of oxygen and the similarity in thermal properties of N_2 and air, the normalised intensity evaluated from the nitrogen free stream data is solely a function of temperature. The air normalised intensity $\frac{I_{ref}}{I}(p,T)$ is then further normalised by the nitrogen data $\frac{I_{ref}}{I}\left(T\right)$ as shown in Eq. (1).

$$\frac{I_{ref}\left(p\right)}{I\left(p\right)} = \frac{I_{ref}\left(p,T\right)}{I\left(p,T\right)} \frac{I\left(T\right)}{I_{ref}\left(T\right)} \tag{1}$$

6.3. PSP Calibration

To calibrate the PSP signal, the paint applied to the surface is subject to a change in pressure over a desired range whilst illuminated the excitation light source. This is carried out in-situ using the same optical setup as used during the test. This ensures the variation in environmental factors that effect PSP's response are kept to a minimum. The test section is evacuated and then brought back to atmosphere or vice versa. The corresponding intensity change is then normalised by the reference intensity (evaluated at vacuum). Finally, on a pixel by pixel bases, a curve is fit of the form shown in Eq. (2) between the normalised pressure $\frac{p}{p_{ref}}$ and normalised intensity $\frac{I_{ref}}{I}$.

$$\frac{I_{ref}}{I} = X \cdot \left[\frac{p}{p_{ref}}\right]^{Y} + Z \tag{2}$$

Where X, Y and Z are fitting parameters which, on average, were found to be 0.037, 0.334 and 0.952 respectively.

6.4. Evaluation of Drag Augmentation

Once the calibration curve is applied, converting the raw counts to local surface pressure, the drag over the pattern can be evaluated. First, the pressure loading parallel to the flow on each sawtooth F_n is found through the integration and subsequent subtraction of the pressure on the windward and leeward faces respectively shown in Eq. (3).

$$F_n = \int p \cdot \sin\left(\theta\right) dA \tag{3}$$

where dA is the area of a pixel projected onto the surface of the sawtooth and θ is the local surface inclination on the sawtooth element.

The total stress au_p experienced over the full FoV of the camera is then the sum of the forces exerted over each sawtooth normalised by the smooth plate area over which they act.

$$\tau_p = \frac{\sum_{n=1}^{N} F_n}{A_{fp}} = \frac{F_r}{A_{fp}}$$
 (4)

where N is the total number of sawtooth elements in the camera's FoV.

Following this, the drag coefficient can then be found by normalising τ_p by the free stream dynamic pressure shown in Eq. (5).

$$C_d = \frac{\tau_p}{\frac{1}{2}\rho_\infty u_\infty^2} \tag{5}$$

Lastly, the augmentation is evaluated by normalising by the smooth wall skin friction coefficient C_f calculated using Eq. (6).

$$C_f = \frac{0.370}{F_{C_r}} \cdot log_{10} \left(\frac{Re}{F_{Re}}\right)^{-2.584} \tag{6}$$

where F_{C_r} and F_{Re} are correction factors to account for compressibility effects defined as shown in Eq. (7) and Eq. (8) respectively.

$$F_{C_r} = \frac{T_{ref}}{T_{\infty}} \tag{7}$$

$$F_{Re} = \frac{\mu_{ref} T_{ref}}{\mu_{\infty} T_{\infty}} \tag{8}$$

Here μ_{ref} is the reference viscosity at the reference temperature T_{ref} calculated using Eq. 9

$$T_{ref} = T_{\infty} \cdot \left[1 + 0.032 \cdot M^2 + 0.58 \left(\frac{T_{wall}}{T_{\infty}} - 1 \right) \right]$$
 (9)

7. Results & Discussion

Figure.8 shows the pressure contours over the surface for each condition. Interestingly, it can be seen that the pressure field develops over the roughness pattern. The peak values diminish as you move downstream settling to only minor variations at around 24mm from the start of the camera's FoV, approximately 100mm from the start of the pattern. This development is a consequence of the thickening of the boundary layer as the flow responds to the surface. Initially, the sawtooth elements protrude further into the boundary layer resulting in a substantial overshoot in surface pressure around the peak of teeth. Gradually, the boundary layer grows reducing the proportion occupied by the roughness.

Zooming in, Fig.9 highlights a span wise average pressure profile of a single sawtooth element. The pressure profile over the roughness is seen to form three distinct regions. The first extends from the trough to around 50% of the elements total length ($\bar{x}=0.5$). Here, the local surface pressure sits blow the free stream static pressure at as low as 30% of its value at the trough. Furthermore, this region is mostly unaffected by the changes in flow properties, as the discrepancies between conditions C1 to C3 are minimal, appearing only at around $\bar{x}=0.4$. This can be attributed to circulation regions common in regularly spaced roughness patterns like those in [33, 34, 35]. The flow then reattaches to the sawtooth element, resulting in a large increase in surface pressure to a maximum value just prior to the patterns peak at $\bar{x}\approx 0.8$. This region is much more sensitive to the free stream conditions, with the maximum reducing from 4 times the smooth plate value at condition C1 to under 3 times at condition C3. This peak is followed by rapid decrease in pressure on the peak and leeward face of the sawtooth clearly as a consequence of the flow separating.

Figure.10 plots the integrated drag force highlighting the influence of each sawtooth segment. Although the flow exerts a larger pressure on the windward face, the windward angle of 25 degrees results in a much smaller fraction of that pressure contributes to the drag. On the other hand, despite only occupying 20% of the sawtooth length, a much larger fraction of the leeward pressure field resists the windward force, quickly reducing the cumulative drag force.

7.1. Comparison of PSP to Force Balance

The pressure data was converted to a drag coefficient and the force balance data to a friction coefficient as described in sections 6.4 and Ref.[26]. Figure.11 plots both against the Reynolds number evaluated at the centre of the test piece. The measured skin friction on the smooth plate is captured well by the turbulent Eckert correlation for each condition. Secondly, there is a marked increase in the skin friction observed over the sawtooth surface which reduces substantially with Reynolds number. Furthermore, there is good agreement between the PSP and force balance measurements with the pressure drag data sitting below the friction coefficient data. Figure.12 highlights this discrepancy by plotting the

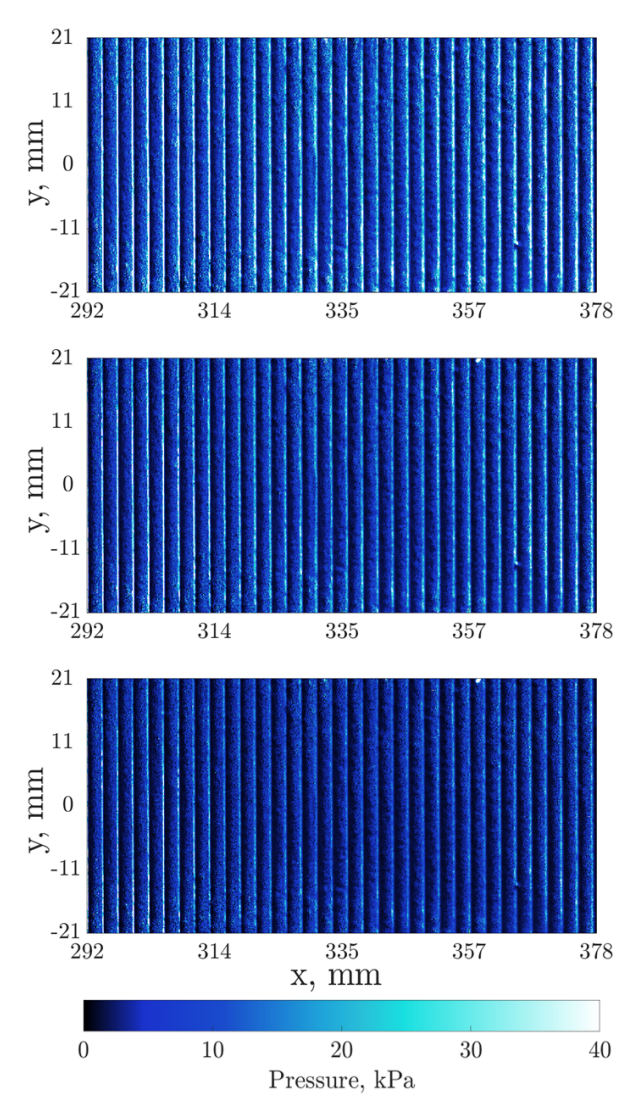


Fig 8. Surface pressure field over the ST25 roughness pattern for conditions C1 - C3.

percentage difference between the two data sets against k/δ . It can be seen that a signifiant fraction of the shear augmentation results from pressure drag. By comparison the viscous shear over these elements is seen to be of the order of 1% of the total force exerted. This can be explained by the flow field being largely separated over the sawtooth as seen in the pressure profiles Fig.9. A similar result was found in the numerical work of Johnston and Mazaheri over a sinusoidal roughness pattern [36]. The viscous shear was found to be less than smooth wall value over the majority of the patterned surface, likely a consequence of the separation and reattachment of the flow also observed in this work. Additionally the pressure drag component is seen to diminish with k/δ which can be attributed to the reduction in fluid momentum that occupancies the reduction in the size of the roughness elements relative to the boundary layer.

7.2. Shear Stress Augmentation

Figure.13 plots the evaluated shear stress augmentation verse the roughness Reynolds number with the characteristic height set to the physical roughness height of 1mm. Figures.14,15, and 16 plot the same data against equivalent sand grain roughness Reynolds number where k_s is defined by van Rij, Dirling, and Sigal respectively. Additionally, the correlation put forward by Nestler defined in Eq. (10) is

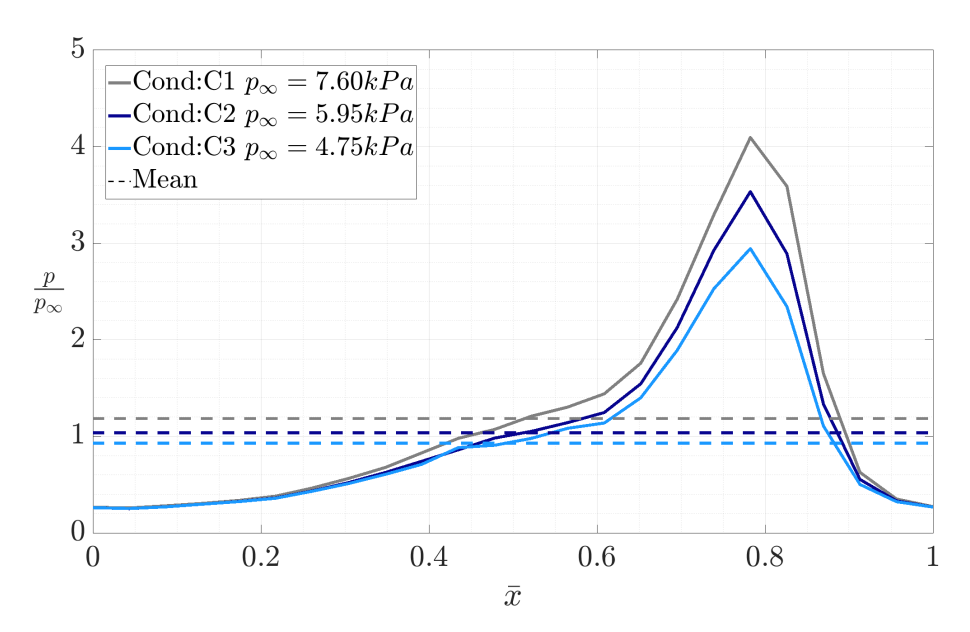


Fig 9. Average pressure distribution over a single sawtooth normalised by the free stream static pressure.

displayed [37]. The correlation is an adaptation of Goddard's work [9]that accounts the non adiabatic wall present during these tests. The substantial increase in shear stress experienced by rough walls is reiterated, with the augmentation factors being 3 to 4 times the smooth wall values. Similarly, the match between both measurement techniques solidifies that pressure drag is the dominant component of the forces over rough walls at this scale.

$$\frac{C_{f_{k+}}}{C_{f_{k+-0}}} = \left[0.365 \frac{T_w}{T_r} + 0.635\right] \log_{10}\left(k^+\right) \tag{10}$$

Where k^+ retains its typical definition shown in Eq. (11).

$$k^{+} = \frac{\rho U_{\tau} k}{\mu} \tag{11}$$

with the friction velocity U_{τ} defined as in Eq.12 where τ_w is the smooth wall shear stress.

$$U_{\tau} = \sqrt{\frac{\tau_w}{\rho}} \tag{12}$$

Moreover, it is shown that the agreement to the Nestler correlation varies significantly with the definition of roughness Reynolds number. When defined using the physical roughness height, the measured augmentation sits significantly above the augmentation predicted by Nestler. The agreement is improved by the use of the equivalent sand-grain roughness height, with the strongest agreement stemming from the use of Sigal's definition for k_s . It is possible that this result is a consequence of how each equivalent sand-grain roughness correlation was developed. van Rij and Dirling opted for the use various spherical segments and hemispheres where as Sigal's is defined by two dimensional bars more similar to the two dimensional sawtooth pattern. This variability questions how applicable sand-grain roughness correlations are to hypersonic flow fields and highlights the uniqueness of flow around different roughness topologies. Lastly, regardless of k^+ definition, the trend of the measured data opposes the generally

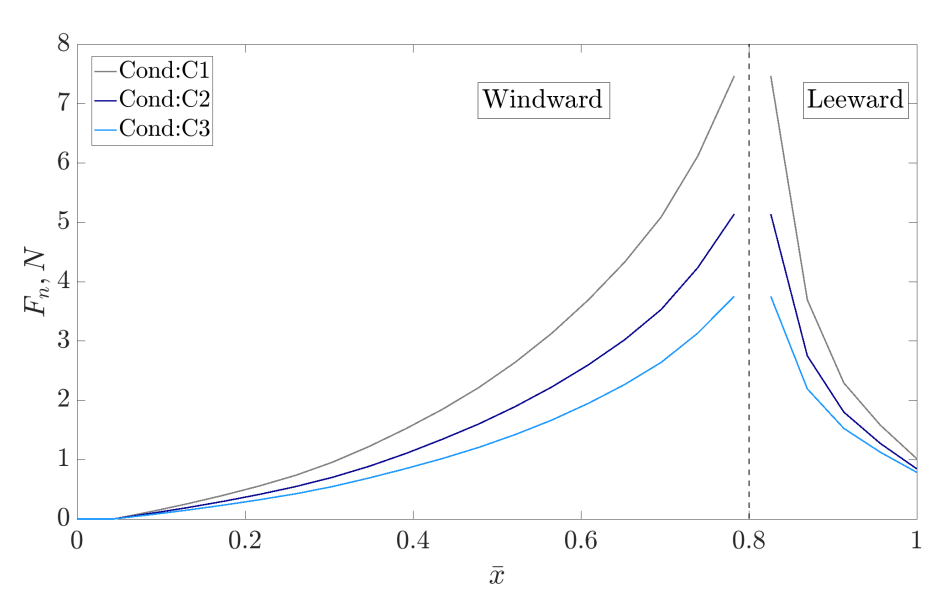


Fig 10. Cumulative drag force over the sawtooth element at each flow condition.

excepted pattern of increasing skin friction augmentation factors with increasing k^+ . This is likely a direct result of the observed augmentation being primarily pressure drag and the flow being more akin to flow over obstacles [38].

8. Conclusion

In conclusion, this paper presented pressure sensitive paint as a method to provide a two dimensional map detailing the pressure field around the roughness elements and ultimately determine the pressure drag experienced in hypersonic flow. A good agreement between the PSP evaluated drag coefficient and the skin friction coefficient determined through the use of a floating force balance was found. This experimentally validates the theory that, at these roughness scales, pressure drag is the predominant factor in augmenting the shear stress over the surface. Further comparison of the data to the Nestler correlation showcases the sensitivity of k^+ definition on determining augmentation factors and questions the generality of sand-grain roughness in hypersonic flow. Finally, C_d augmentation is shown to decrease with both the k^+ and Re_x differing from the correlation presented. This difference eludes to the possible break down of typical rough wall behaviour to effects more similar to flow over obstacles for the sawtooth pattern $k/\delta > 0.2$.

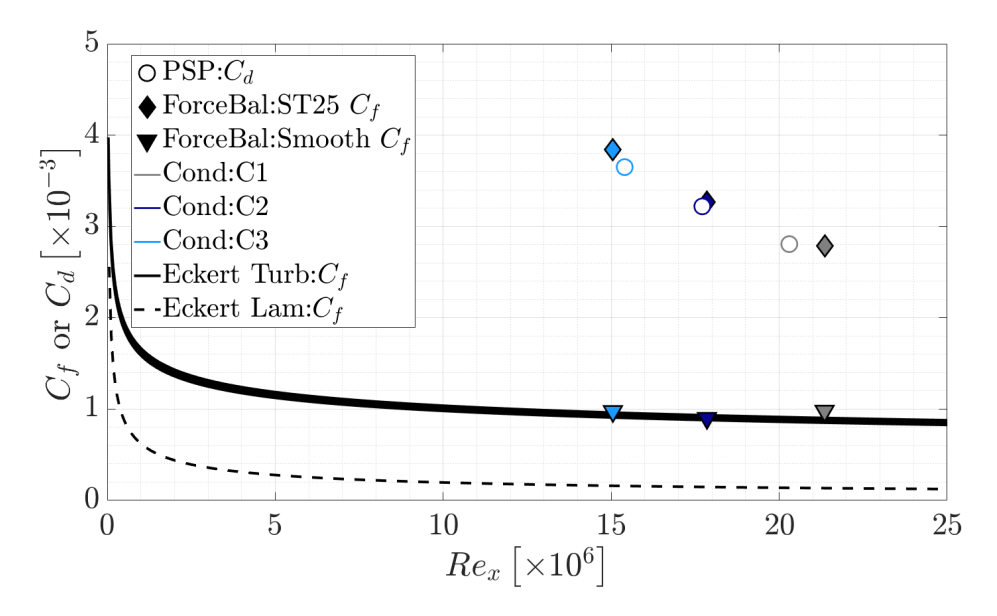


Fig 11. Comparison of PSP evaluated drag coefficient and friction factor for the ST25 roughness pattern.

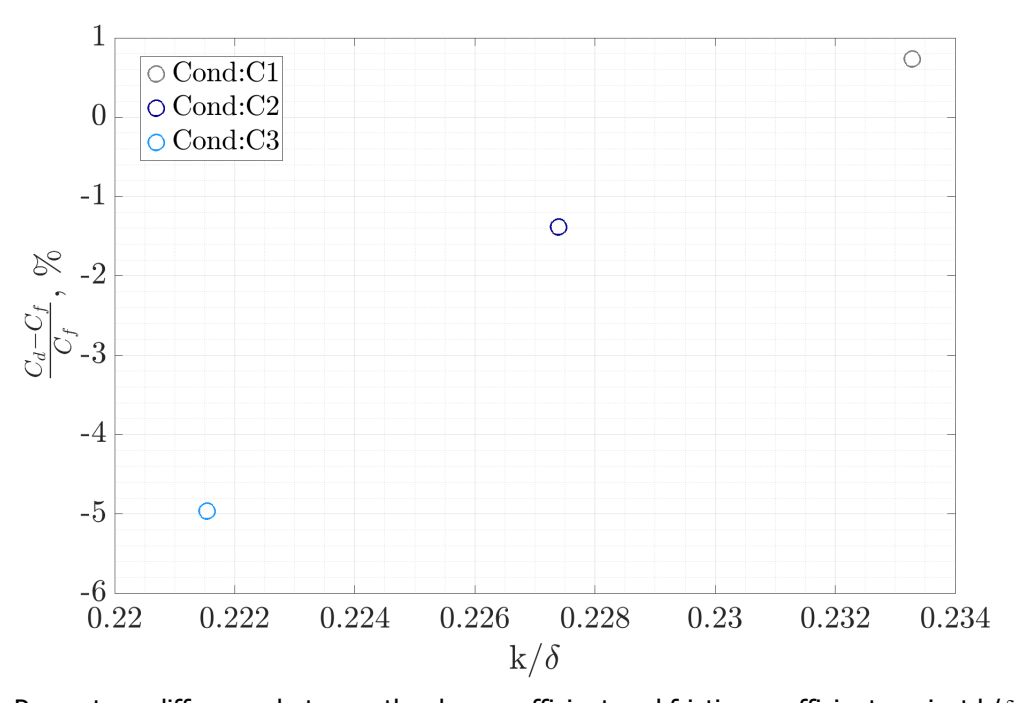


Fig 12. Percentage difference between the drag coefficient and friction coefficient against k/δ for each condition.

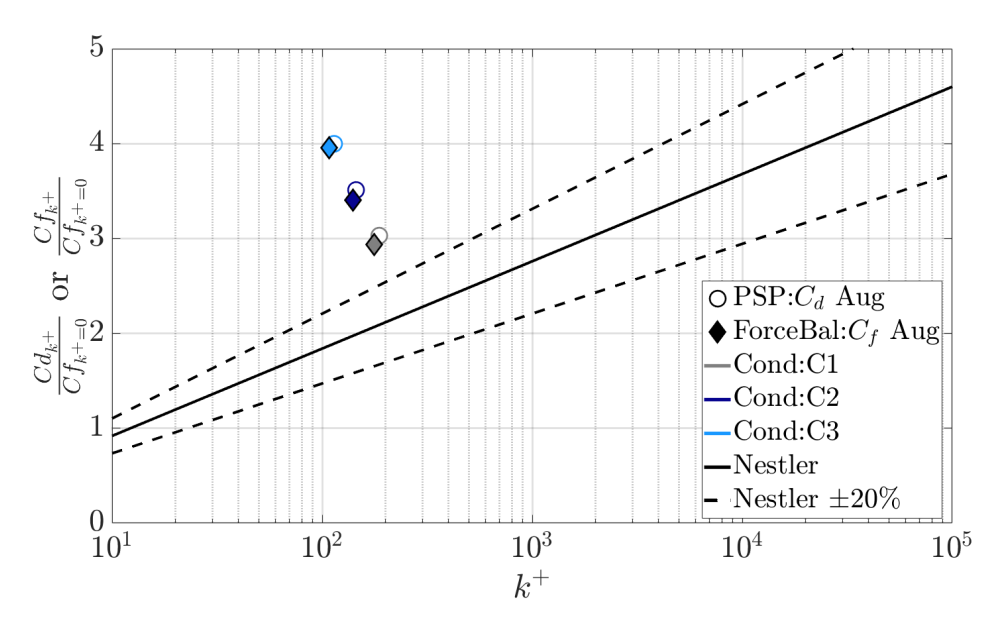


Fig 13. Skin friction Augmentation for the ST25 verse roughness Reynolds number.

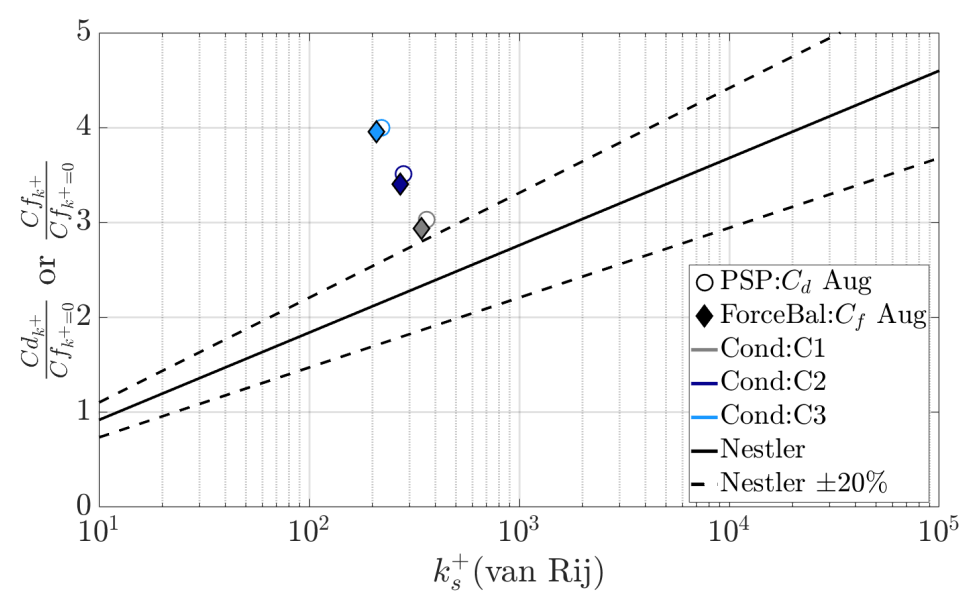


Fig 14. Skin friction Augmentation for the ST25 verse equivalent sand-grain roughness Reynolds number defined by van Rij.

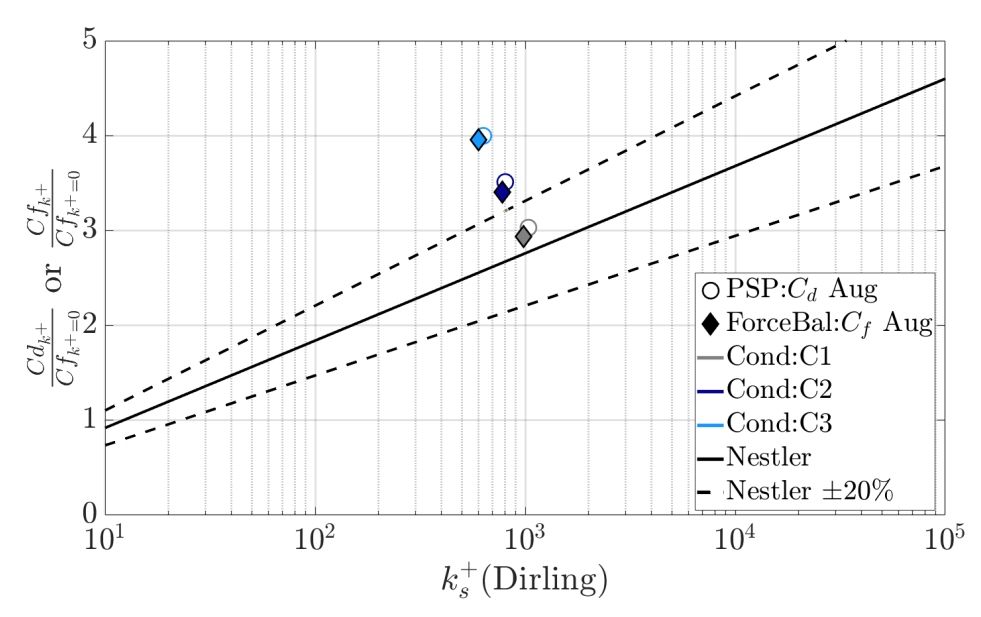


Fig 15. Skin friction Augmentation for the ST25 verse equivalent sand-grain roughness Reynolds number defined by Dirling.

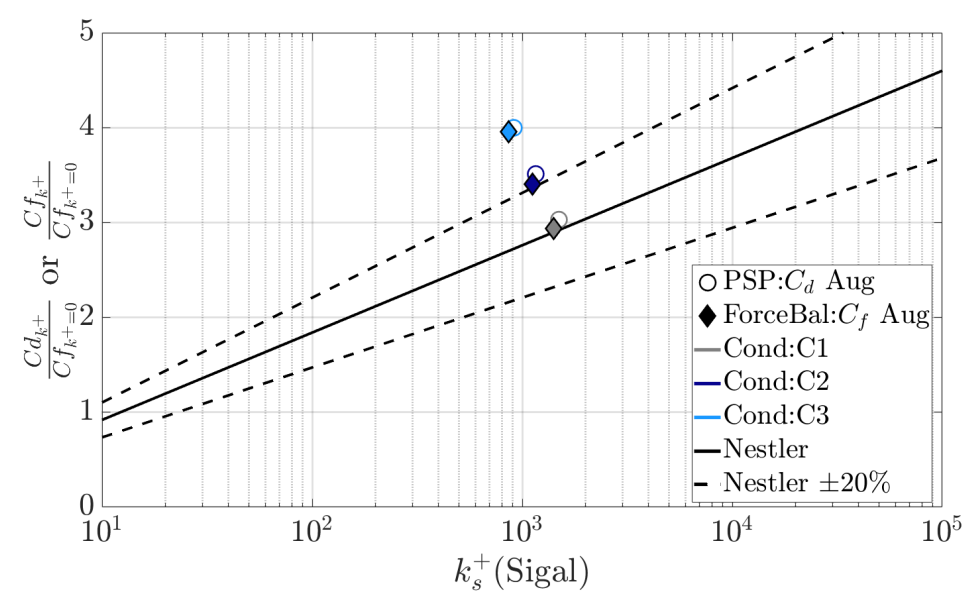


Fig 16. Skin friction Augmentation for the ST25 verse equivalent sand-grain roughness Reynolds number defined by Sigal.

Acknowledgments

The authors would like to extend gratitude to Andrea Dabija and Gabriel Tansley for use and supervision of the instrumentation workshop facilities, Albert Williams and Callum Turner for the operation of the Oxford High Density tunnel, and Raghul Ravichandran for his expertise in porous media.

References

- [1] Vignoles, G.L., Lachaud, J., Aspa, Y., Goyhénèche, J.M.: Ablation of carbon-based materials: Multiscale roughness modelling. Composites Science and Technology, 69(9):1470–1477 (2009). URL http://dx.doi.org/https://doi.org/10.1016/j.compscitech.2008.09.019. Special Issue on the 12th European Conference on Composite Materials (ECCM12), organized by the European Society for Composite Materials (ESCM)
- [2] Fitzer, E., Manocha, L.M.: Carbon Reinforcements and Carbon/Carbon Composites, chap. 10, pp. 310–336. Springer Berlin, Heidelberg (1998)
- [3] Schneider, S.P.: Effects of Roughness on Hypersonic Boundary-Layer Transition. Journal of Spacecraft and Rockets, 45(2):193–209 (2008). URL http://dx.doi.org/10.2514/1.29713
- [4] Corke, T.C., Bar-Sever, A., Morkovin, M.V.: Experiments on transition enhancement by distributed roughness. The Physics of Fluids, 29(10):3199–3213 (1986). URL http://dx.doi.org/10.1063/1.865838
- [5] Price, K.J., Panerai, F., Borchetta, C.G., Hardy, J.M., Martin, A., Bailey, S.C.: Arc-jet measurements of low-density ablator spallation. Experimental Thermal and Fluid Science, 133:110544 (2022). URL http://dx.doi.org/https://doi.org/10.1016/j.expthermflusci.2021.110544
- [6] Kryvoruka, J.K., Bramlette, T.T.: Effect of Ablation-Induced Roll Torques on Reentry Vehicles. Journal of Spacecraft and Rockets, 14(6):370–375 (1977). URL http://dx.doi.org/10.2514/3.57211
- [7] Nikuradse, J.: Law of flows in rough pipes, English Translation. NACA TM 1292 (1950)
- [8] Schlichting, H.: Experimental Investigation of the problem of surface roughness (1936)
- [9] Goddard, F.E.: Effect of Uniformly Distributed Roughness on Trubulent Skin-Friction Drag at Supersonic Speeds. Journal of the Aerospace Sciences, 26(1):1–15 (1959). URL http://dx.doi.org/10.2514/8.7911
- [10] Young, F.: Experimental Investigation of the Effects of Surface Roughness on Compressible Turbulent Boundary Layer Skin Friction and Heat Transfer (1965)
- [11] Wade, J.: An Experimental investigation of Effects of Surface Roughness on the Drag of a Cone-Cylinder Model at a Mach Number of 2.48 (1955)
- [12] Reda, D.C., Ketter, F.C., Fan, C.: Compressible Turbulent Skin Friction on Rough and Rough/ Wavy Walls. AIAA Journal, 13(5):553–554 (1975). URL http://dx.doi.org/10.2514/3.49761
- [13] Bowersox, R.: Survey of High-Speed Rough Wall Boundary Layers: Invited Presentation (2012). URL http://dx.doi.org/10.2514/6.2007-3998
- [14] Holden, M.: Experimental studies of surface roughness shape and spacing effects on heat transfer and skin friction in supersonic and hypersonic flows (1984). URL http://dx.doi.org/10.2514/6.1984-16
- [15] Powars, C.A.: Passive Nosetip Technology (PANT) Program, Interim Report, Vol. III Part II -Roughness Augmented Heating Data Correlation and Analysis (1974)
- [16] Wright, M., Edquist, K., Tang, C., Hollis, B., Krasa, P., Campbell, C.: A Review of Aerothermal Modeling for Mars Entry Missions (2010). URL http://dx.doi.org/10.2514/6.2010-443

- [17] Wilder, M.C., Prabhu, D.K.: Rough-Wall Turbulent Heat Transfer Experiments in Hypersonic Free Flight (2019). URL http://dx.doi.org/10.2514/6.2019-3009
- [18] Hambidge, C., Steuer, D.C., Condren, W.J., McGilvray, M.: Roughness Induced Heat Transfer and Shear Stress Augmentation Measurements of the HEEET Thermal Protection System. AIAA SCITECH 2024 Forum. AIAA (2024). URL http://dx.doi.org/10.2514/6.2024-0444
- [19] Asai, K., Kanda, H., Cunningham, C., Erausquin, R., Sullivan, J.: Surface pressure measurement in a cryogenic wind tunnel by using luminescent coating. ICIASF'97 Record. International Congress on Instrumentation in Aerospace Simulation Facilities, pp. 105–114 (1997). URL http://dx.doi.org/10.1109/ICIASF.1997.644671
- [20] Sakaue, H.: Porous pressure sensitive paints for aerodynamic applications. Ms thesis, School of Aeronautics and Astronautics, Purdue University, West Lafayette IN (1999)
- [21] Sakaue, H., Sullivan, J.P., Asai, K., Iijima, Y., Kunimasu, T.: Anodized aluminum pressure sensitive paint in cryogenic wind tunnels. I.S. of America, editor, Proceedings of the 45th International Instrumentation Symposium, pp. 337–346 (1999)
- [22] Ewenz Rocher, M., Hermann, T., McGilvray, M.: Pressure-sensitive paint diagnostic to measure species concentration on transpiration-cooled walls. Exp Fluids, 63(2) (2022). URL http://dx.doi.org/0.1007/s00348-021-03355-9
- [23] Sakaue, H., Sullivan, J.P.: Time Response of Anodized Aluminum Pressure-Sensitive Paint. AIAA Journal, 39(10):1944–1949 (2001). URL http://dx.doi.org/10.2514/2.1184
- [24] Sakaue, H.: Luminophore application method of anodized aluminum pressure sensitive paint as a fast responding global pressure sensor. Review of Scientific Instruments, 76(8):084101 (2005). URL http://dx.doi.org/10.1063/1.1988007
- [25] Sakaue, H., Ishii, K.: Optimization of Anodized-Aluminum Pressure-Sensitive Paint by Controlling Luminophore Concentration. Sensors, 10(7):6836–6847 (2010). URL http://dx.doi.org/10.3390/s100706836
- [26] Steuer, D.C., Hambidge, C., McGilvray, M.: A Method for Direct Shear Measurement of Large Scale Roughened Surfaces in Short Duration Hypersonic Facilities. AIAA SCITECH 2023 Forum. AIAA (2023). URL http://dx.doi.org/10.2514/6.2023-2442
- [27] Paige, C.C., Saunders, M.A.: Algorithm 583: LSQR: Sparse linear equations and least squares problems. ACM Transcations on Mathematical Software (TOMS), 8(2):195–209 (1982)
- [28] Wylie, S., Doherty, L., McGilvray, M.: Commissioning of the Oxford High Density Tunnel (HDT) for boundary layer stability measurements at Mach 7. 2018 Fluid Dynamics Conference. American Institute of Aeronautics and Astronautics (2018)
- [29] McGilvray, M., Doherty, L.J., Neely, A.J., Pearce, R., Ireland, P.: The Oxford High Density Tunnel. 20th AIAA International Space Planes and Hypersonic Systems and Technologies Conference. AIAA (2015). URL http://dx.doi.org/10.2514/6.2015-3548
- [30] van Rij amd B J Belnap, J.A., Ligrani, P.M.: Analysis and Experiments on Three-Dimensional, Irregular Surface Roughness. Journal of Fluids Engineering, 124(3):671–677 (2002). URL http://dx.doi.org/10.1115/1.1486222
- [31] R. Dirling, J.: A method for computing roughwall heat transfer rates on reentry nosetips. 8th Thermophysics Conference. AIAA (2005). URL http://dx.doi.org/10.2514/6.1973-763
- [32] Sigal, A., Danberg, J.E.: New correlation of roughness density effect on the turbulent boundary layer. AIAA Journal, 28:554–556 (1990). URL http://dx.doi.org/10.2514/3.10427
- [33] Neeb, D., Gülham, A., Merrifield, J.A.: Rough-Wall Heat Flux Augemtation Analysis Within the ExoMars Project. Journal of Spacecraft and Rockets, 163(1) (2016)

- [34] Leonardi, S., Orlandi, P., Antonia, R.A.: Properties of d- and k-type roughness in a turbulent channel flow. Physics of Fluids, 19(12):125101 (2007). URL http://dx.doi.org/10.1063/1.2821908
- [35] Perry, A.E., Schofield, W.H., Joubert, P.N.: Rough wall turbulent boundary layers. Journal of Fluid Mechanics, 37(2):383–413 (1969). URL http://dx.doi.org/10.1017/S0022112069000619
- [36] Johnston, C.O., Mazaheri, A.: An Approach for Practical Grid-Resolved Roughness Aerothermodynamic Simulations for Woven Heatshield Surfaces (2025). URL http://dx.doi.org/10.2514/6.2025-0825
- [37] Nestler, D.: Compressible turbulent boundary-layer heat transfer to rough surfaces. AIAA Journal, 9(9):1799–1803 (1971)
- Over [38] Jiménez, J.: Turbulent Flows Rough Walls. Annual Re-Fluid 36(Volume 36, 2004):173-196 **URL** view of Mechanics, http://dx.doi.org/https://doi.org/10.1146/annurev.fluid.36.050802.122103